Simulation of noble metal particle growth and removal in the molten salt fast reactor

Edo Frederix[1], **Ed Komen**[1]
[1]Nuclear Research and Consultancy Group (NRG),
Westerduinweg 3, 1755 LE, Petten,
the Netherlands

Abstract

In the Molten Salt Fast Reactor (MSFR), fuel is dissolved in a liquid salt, causing the formation and decay of fission products, such as noble metals, inside the salt. Noble metals have very low solubility and do not dissolve in the salt. They are known to agglomerate into particles which, in turn, diffuse, drift or sediment to interfaces such as walls, free surfaces and bubbles, where they deposit. Leveraging this in the MSFR, online or offline helium bubbling is foreseen to act as a means to extract noble metal particles from the salt. This can potentially limit strong deposition of particles onto walls (i.e., plating), preventing dangerous decay heat hotspots in the heat exchangers or other primary circuit components. In this paper, we investigate the efficiency of particle removal by helium bubbles in the MSFR using CFD modelling. Theoretical estimates of equilibrium particle size distributions are used as initial condition. CFD calculations are performed in a simplified MSFR geometry. Bubble expansion, turbulent bubble coalescence and turbulent break-up are accounted for using the poly-disperse LogMoM model [1], embedded in the two-fluid framework in OpenFOAM. The CFD analyses presented in this paper, in conjunction with the developed theory of noble metal particle formation, growth and capture, will help in the understanding and optimization of the fuel cycle in the MSFR or any other molten salt reactor design. The precise knowledge of how noble metal particle populations in the salt can be controlled, and how plating of noble metal particles onto primary circuit reactor components can be reduced, contributes to safe molten salt reactor operation.

Introduction

In the Molten Salt Fast Reactor (MSFR) [2], fuel is dissolved in a liquid salt, causing the formation and decay of fission products inside the salt. Some of these fission products are salt seekers and dissolve in the salt by forming stable bonds with fluorine. Other products, being noble gases and noble metals, have very low solubility and do not dissolve in the salt [3]. Noble metal atoms are known to agglomerate into particles which, in turn, diffuse, drift or sediment to interfaces such as walls, free surfaces and bubbles, where they deposit. Leveraging this in the MSFR, online or offline helium bubbling is foreseen to act as a means to extract noble metal particles from the salt [4]. This can potentially limit plating, preventing dangerous decay heat hot spots in the heat exchangers or other primary circuit components. However, currently the knowledge on the quantitative behavior of noble metal particles in the MSFR is unknown from both an experimental as well as modeling point of view.

The mechanics of noble metal particle flotation in the MSFR, as it is currently understood, involves a complex interplay of noble metal atom formation by fission and decay, particle growth by coagulation, and particle capture by interfaces driven by Brownian diffusion, sedimentation or interception. Particle capture efficiency depends strongly on particle size. Small particles, having a diameter in the range of the nanometer scale, tend to diffusive more efficiently towards bubbles due to Brownian motion [5]. Larger particles, in the range of the micrometer scale and beyond, tend to sediment or drift due to inertial effects towards bubbles more efficiently [6]. The balance of this interplay of physics determines key integral properties of the system such as equilibrium particle size and noble metal atom cycle time, the latter being an import input parameter to salt inventory calculations.

In this paper, we investigate the efficiency of particle removal by helium bubbles in the MSFR using CFD modelling. At steady-state operation, an estimate of the noble metal particle population can be calculated using homogeneous theory [7], incorporating particle formation, growth and removal. However, this theory depends on the behavior of helium bubbles in the MSFR, in terms of mean void fractions and bubble sizes. Preliminary CFD calculations are performed in a simplified MSFR geometry, in order to compute the mean bubble void fraction and size as a function of superficial inlet velocity and inlet size. Bubble expansion, turbulent bubble coalescence and turbulent break-up are accounted for using the poly-disperse LogMoM model [1], embedded in the two-fluid framework in OpenFOAM. A large number of CFD simulations spanning the input parameter space produce a correlation between superficial bubble inlet velocity on one hand, and the mean bubble void fraction and mean particle size on the other. In turn, this correlation is used to calculate the equilibrium noble metal particle size distribution residing in the reactor at steady-state conditions, from homogeneous theory. Finally, these size distributions are used as initial condition for transient CFD simulations, incorporating both diffusional and hydrodynamic flotation. From the decay rate of noble metal mass in the system, cycle times may be inferred.

The CFD analysis presented in this paper, in conjunction with the developed theory of noble metal particle formation, growth and capture, will help in the understanding and optimization of the fuel cycle in the MSFR or any other molten salt reactor design. The precise knowledge of how noble metal particle populations in the salt can be controlled, and how plating of noble metal particles onto primary circuit reactor components can be reduced, contributes to safe molten salt reactor operation.

Three-phase flotation model

The problem of noble metal particle flotation is essentially governed by the interaction of three phases: gas bubbles, liquid molten salt and solid noble metal particles. To model this three-phase system, a combination of numerical methods is made. This is described in [8]. Here, we briefly recollect the main features of the three-phase flotation model.

Conservation equations for mass, momentum, energy and particles

For the gas−liquid mixture, the two-fluid model is adopted. The two-fluid model, retaining a full coupling between both phases, is needed because compressibility of bubbles may play an important role in the fluid mechanics of an MSR design as a whole [9] and because the coupling between salt and gas will be strong as a result of high void fractions. The behavior of noble metal particles, on the other hand, is modeled using a passive Eulerian approach that is one-way coupled to the gas−liquid mixture. This is a reasonable simplification because the volume fraction of particles in the reactor is expected to be extremely small making the salt and bubbles relatively unaware of the presence of particles, thus requiring no explicit coupling between particles on one hand and the gas–liquid mixture on the other.

Starting with the two-fluid model [10], we identify the liquid salt phase ℓ and the gas phase g, which have a local volume fraction α, velocity $\mathbf{u}$ and mass density ρ. For $k \in (\ell,g)$, we have an equation for the conservation of mass, i.e.,

$$\frac{\partial \rho_k \alpha_k}{\partial t} + \nabla \cdot (\rho_k \alpha_k \mathbf{u}_k) = \Lambda_k, \tag{1}$$

with interfacial mass transfer term Λ_k which is zero for helium bubbles in salt. Next, we have an equation for the conservation of momentum, i.e.,

$$\frac{\partial \rho_k \alpha_k \mathbf{u}_k}{\partial t} + \nabla \cdot (\rho_k \alpha_k \mathbf{u}_k \mathbf{u}_k) = -\alpha_k \nabla p + \nabla \cdot \left[\alpha_k (\mathbf{T}_k + \mathbf{T}_k^t\right] + \rho_k \alpha_k \mathbf{g} + \mathbf{M}_i, \tag{2}$$

with phase k viscous and turbulent stress tensors $\mathbf{T}_k$ and $\mathbf{T}_k^t$, respectively, mixture pressure p, gravitational acceleration $\mathbf{g}$ and phase k interfacial momentum transfer term $\mathbf{M}_k$ which also satisfies $\mathbf{M}_\ell = \mathbf{M}_g$. Finally, the phase k energy conservation equation is given by

$$\frac{\partial \rho_k \alpha_k e_k}{\partial t} + \nabla \cdot (\alpha_k \rho_k e_k \mathbf{u}_k) = -\nabla \cdot \left[\alpha_k (\mathbf{q}_k + \mathbf{q}_l^t\right] + \nabla \cdot (\alpha_k \boldsymbol{\tau}_k \cdot \mathbf{u}_k) + \rho_k \alpha_k \mathbf{g} \cdot \mathbf{u}_k + E_k, \tag{3}$$

with phase k internal energy e_k, laminar and turbulent heat fluxes $\mathbf{q}_k$ and $\mathbf{q}_k{}^t$, total stress tensor $\boldsymbol{\tau}_k = -p_k\mathbf{I}_k + \mathbf{T}_k$ and interfacial energy transfer term E_k which, just like the interfacial mass and momentum transfer terms, satisfies $E_\ell = -E_g$. The system (1–3) is closed by the selection of a suitable equation of state, constitutive relations for the viscous stress tensor and heat flux, a turbulence model for the turbulent stress and turbulent heat flux and appropriate models for the interfacial mass, momentum and energy transfer terms. The selection of these models will be discussed later on. For more details on the two-fluid model, the reader is referred to Ishii & Hibiki [10] or Drew & Passman [11].

Noble metal particles are modeled in a poly-disperse way, meaning that the full size distribution of particles is considered. We distinguish between a ‘free’ particle population $n_f(d)$ of which member particles are suspended in the salt and are free to diffuse or sediment, and a ‘captured’ particle population $n_c(d)$ of which member particles are attached to a bubble and move along with that bubble. Here, d is

the particle diameter. We use a simple sectional discretization of the particle size domain, so that both distributions are represented by a finite collection of Dirac delta functions, each of which describing the concentration of particles at a distinct and fixed particle diameter d_i. More precisely, if we let $n_j(d)$ be a population with $j \in (f,c)$ defined in such a way that $n_j(d)\mathrm{d}d$ gives the total number of type j particles per unit volume in the size range $[d, d + \mathrm{d}d]$, then it is approximated by

$$n_j(d) = \sum_i N_{i,j}\delta(d_i - d), \tag{4}$$

with $N_{i,j}$ the number concentration of type j particles having size d_i. Conversely, if we integrate $n_j(d)$ over a section defined by, for example, the range $[(d_{i\text{-}1} + d_i)/2, (d_i + d_{i+1})/2]$, then we obtain $N_{i,j}$. Such an integration can be applied to the population balance equation modeling the dynamics of the complete population (e.g., see [12−14]), and results in

$$\frac{\partial N_{i,j}}{\partial t} + \nabla \cdot (\mathbf{v}_{i,j} N_{i,j}) = \nabla \cdot (D_{i,j} \nabla N_{i,j}) + S_{i,j}, \tag{5}$$

with particle velocity $\mathbf{v}_{i,j}$, particle diffusivity $D_{i,j}$ and source term $S_{i,j}$, all three for type j particles in section i. The velocity of free particles must be modeled by taking into account their inertia, drag imposed by salt, gravity and other forces exerted onto the particles. Moreover, the free particle velocity is a function of particle size. A simple algebraic 'local equilibrium' model for the particle velocity can be used, incorporating inertia, Stokes drag and gravity, see [8]. It is given by

$$\mathbf{v}_{i,f} = \mathbf{u}_\ell + [(1 - \rho_\ell/\rho_p)\mathbf{g} - \mathrm{d}\mathbf{u}_\ell/\mathrm{d}t)]\,\tau_p, \tag{6}$$

with particle mass density ρ_p and Stokes relaxation time τ_p. This model is suitable only for very low particle Reynolds numbers, an assumption which is expected to hold because particles will not exceed the micron scale. The free particle diffusivity can be modeled using the Stokes-Einstein relation. Captured particles move with the gas phase, meaning that $\mathbf{v}_{i,c} = \mathbf{u}_g$ and $D_{i,c} = 0$ for all i. Finally, the source term $S_{i,j}$ accounts for the transfer of particles between the free and the captured populations, through flotation. Additionally, it can also account for new particle formation due to precursor decay or fission, loss due to decay, or changes in the population due to particle coagulation. However, in this work these contributions are ignored, as we will only consider the removal rates of particles from an initial population that is at an equilibrium as predicted by homogeneous theory. Returning to the process of particle transfer by flotation, the source term for free particles can be modeled as [6]

$$S_{i,f} = -(H_i P_{\mathrm{col},i} P_{\mathrm{ad},i} P_{\mathrm{stab},i} + D_i) N_{i,f} N_b, \tag{7}$$

with H_i the hydrodynamic flotation rate, D_i the diffusive flotation rate, N_b the number concentration of bubbles and $P_{\mathrm{col},i}$, $P_{\mathrm{ad},i}$ and $P_{\mathrm{stab},i}$ the efficiencies of collision, adhesion and stabilization, which will be explained momentarily. The hydrodynamic flotation part of (7) represents 'classical' flotation by means of particle inertia and sedimentation leading to interception, which is relevant for relatively large particles with sizes just below the micro scale and beyond. The diffusive flotation part is not as commonly considered in flotation theory, and is relevant mostly for relatively small particles with sizes around the micro scale and below (for example, see [5]). The source term for captured particles is simply given by $S_{i,c} = -S_{i,f}$. Next, we will shortly discuss the models for hydrodynamic and diffusional flotation.

Hydrodynamic and diffusional flotation theory

Starting from classical hydrodynamic flotation theory, if we consider a spherical bubble then the rate at which it would collect particles if those particles were not to change trajectory is given by [6]

$$H_i = \frac{\pi}{4}(d_b + d_i)^2 |\mathbf{v}_{i,f} - \mathbf{u}_g|. \tag{8}$$

with bubble diameter d_b, which is simply the frontal area of interception of the bubble multiplied by the relative velocity magnitude. This would be the ideal rate of flotation. In practice, particles will be pushed away by the salt flow around the bubble, reducing the number of particles in the path of the bubble that will collide with it. To account for this, the collision efficiency P_{col} is introduced. Subsequently, when particles collide with a bubble, they may not necessarily attach to the bubble. The fraction of particles colliding with the bubble and attaching to it is usually smaller than unity, and is modeled by $P_{\text{ad},i}$. Finally, attached particles can form a bond with the bubble that is not stable and may be shed by the bubble again. This is accounted for by the efficiency of stabilization, $P_{\text{stab},i}$. All these three efficiencies are subject to a vast amount of flotation research, e.g., see Nguyen & Schulze [6]. Here, we use the model of Yoon & Luttrell [15] for P_{col} and $P_{\text{ad},i}$. This model is applicable to finite non-zero Reynolds number flow around the bubbles. Moreover, we assume that the efficiency of stabilization, $P_{\text{stab},i}$, is unity as a result of the low solubility of noble metals in salt. Thus, we have

$$P_{\text{col},i} = \frac{3}{2}\left(1 + \frac{8\text{Re}_b^{0.72}}{45}\right)\frac{d_i^2}{d_b^2}, \tag{9}$$

$$P_{\text{ad},i} = \sin^2\left[2\ \arctan\left\{\exp\left(-P_{\text{col},i}\Gamma_i\frac{d_b}{d_i}\right)\right\}\right] \qquad \text{and} \tag{10}$$

$$P_{\text{stab},i} = 1 \tag{11}$$

with bubble Reynolds number Re_b and the non-dimensional coefficient Γ_i given by

$$\Gamma_i = \frac{2|\mathbf{u}_g - \mathbf{u}_\ell|\tau_i}{d_i + d_b}, \tag{12}$$

with induction time τ_i. The induction time is essentially a parameter that embodies the complex interplay of microscopic forces acting on the bubble interface, salt and particle leading to adhesion of particles. From the experiments of Dai et al. [16] we have $t_{\text{ind},i} = Ad_i^B$ with $A = 0.05$ and $B = 0.6$.

The diffusional flotation part of (7) is represented by the flotation rate D_i. Following what was done in [7], it is given by

$$D_i = \pi \text{Sh}_i d_b \mathcal{D}_i, \tag{13}$$

with Sherwood number Sh_i and particle diffusivity $\mathcal{D}_i$. The diffusivity is given by the Stokes-Einstein relation, i.e.,

$$\mathcal{D}_i = \frac{k_B T}{3\pi\mu_\ell d_i} \tag{14}$$

with Boltzmann's constant k_B, temperature T and salt dynamic viscosity μ_ℓ. The Sherwood number is modeled using the Ranz-Marshall relation [17], given by

$$\mathrm{Sh}_i = 2.0 + 0.6\sqrt{\mathrm{Re}_b}\sqrt[3]{\mathrm{Sc}_i}, \tag{15}$$

with Sc_i the Schmidt number given by $\mathrm{Sc}_i = \nu_\ell / \mathcal{D}_i$ where ν_ℓ is the salt kinematic viscosity. The Ranz-Marshall model was originally developed for evaporating drops, but also holds validity for colloidal mass transfer in light of the diffusive nature of the transfer process. Moreover, in the MSRE it was observed that noble metals migrate according to the simplest form of mass transfer theory [3,18,19], which gives further credence to the validity of this analogy.

Log-normal method of moments for bubbles

Bubbles are injected into the bottom of the reactor vessel at a certain size. Depending on that size, their number and local turbulent conditions, they will undergo coalescence or break-up. Moreover, with decreasing pressures higher up in the vessel, they will expand. Therefore, the evolution of the bubble population subject to these effects must be modeled. For this, we use the Log-normal Method of Moments (LogMoM), developed in [1,20]. The method assumes that the bubble size distribution has a log-normal shape. The log-normal function has three degrees of freedom: its width, height and offset. The function is closed by the solution of three independent moment transport equations (number, interfacial area and volume concentrations) which are obtained from the bubble population balance equation, by integration. The integration of the coalescence and break-up terms is done using Gauss quadrature, which makes the approach very versatile and able to deal with complicated break-up and coalescence kernels. Special attention is paid to the consistent integration of the break-up term, assuring a source term that is always non-negative. From the solution of the three moment equations, LogMoM produces the full bubble size distribution from which the Sauter mean diameter can be calculated. In turn, the Sauter mean diameter is fed to all closure models that require information of the size of bubbles, such as the drag model for bubbles or the hydrodynamic and diffusional flotation rates.

This, then, completes the short description of the main features of the mathematical three-phase model. We now continue with the description of the simulation setup for particle flotation in the MSFR.

Simulation setup of particle flotation in the MSFR

The model as discussed above is implemented in OpenFOAM-9. The two-fluid model is solved using the standard multiphaseEulerFoam solver of OpenFOAM. A separate library called flotationFoam is developed for the modeling of the free and captured particle populations. This library can be dynamically linked against the standard multiphaseEulerFoam solver of OpenFOAM, therewith avoiding any modification of standard OpenFOAM code. In this Section, we describe the simulation setup of particle flotation in the MSFR, using OpenFOAM.

Simplified geometry of the MSFR

The MSFR is envisioned to be a cylindrical vessel in which molten salt is circulated by means of both natural convection and forced convection. Previously, within the EVOL project, studies have been performed on the specific design of the vessel in order to promote mixing and reduce temperature peaking, see for example [21]. This led to a complex design with a curved core cavity shape and a number of radial channels in which a heat exchanger and pump are placed, cooling the salt and re-injecting it again at the bottom of the vessel. The proper simulation of this geometry requires a full three-dimensional mesh of at least one periodic slice of the domain. Instead, here a simplified axisymmetric

geometry is considered, that was also used by Caruggi et al. [22] to study gaseous fission product removal rates. Because of the axial symmetry, it is sufficient that only a two-dimensional wedge of the full geometry is simulated. This two-dimensional wedge is shown in Figure 1. A wedge angle of 5° is chosen, conform OpenFOAM's recommendation for wedge geometry simulations. The domain consists of a vessel cavity (shaded by stripes in Figure 1), which is connected to a pump and heat exchanger region (shaded by blue and red). The dimensions of the geometry are indicated in Figure 1, where it is noted that the inlet and outlet of the heat exchanger and pump channel are equal in height and width. Bubbles are injected from the bottom, and the salt-bubble mixture is allowed to expand into an expansion tank as indicated. Bubbles and captured particles attached to them are removed from the salt mixture once they reach the region shaded in green, such that no bubbles or captured particles are recirculated. The heat exchanger is modeled by a sink term that brings the temperature back to the desired inlet temperature. The effect of the pump is represented by a momentum source that establishes the desired flow rate of salt. The inlet mass flow rate of bubbles is controlled by specification of the inlet velocity $\mathbf{u}_g$ at a constant void fraction of 10%. Boundary conditions are the standard ones for wall bounded flow. At the outlet the pressure is fixed at atmospheric pressure and a zero-gradient condition is applied for the salt and bubble velocity. Conversely, on the inlet both velocities are set while pressure is zero-gradient.

Figure 1: Simplified two-dimensional wedge representation of the MSFR with pump region (red), heat exchanger region (blue and red) and bubble and captured particle remover (green, red and blue). Divisions between mesh blocks are indicated by the thin red lines. The reactor cavity is shaded by the diagonal grey lines.

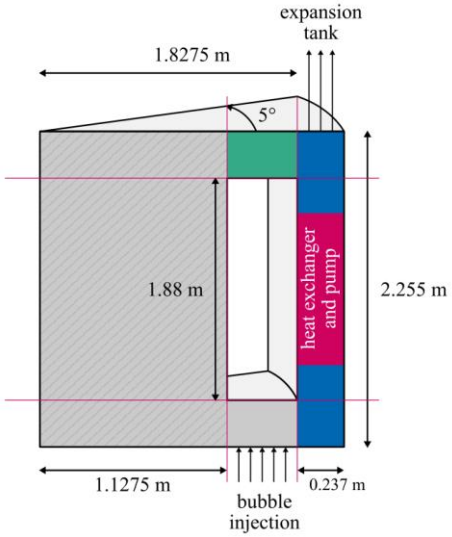

The mesh is constructed using OpenFOAM's blockMesh tool, from the eight blocks that result from the division of the mesh as marked by the thin red lines in Figure 1. Each block is mapped by hexahedral cells in such a way that the mesh density is equal, or very close to, 64 cells/m per spatial direction. In the radial direction, from axis to the outer wall of the heat exchanger and pump, blocks have 72, 44 and 15 cells, respectively. In the axial direction, from bottom to top, blocks have 12, 120 and 12 cells, respectively. This gives a total of 13.584 cells, which is very moderate and allows for long calculations with limited computational effort.

Figure 2: Prompt and decay heat source as obtained from the steady-state results of Caruggi et al. [22].

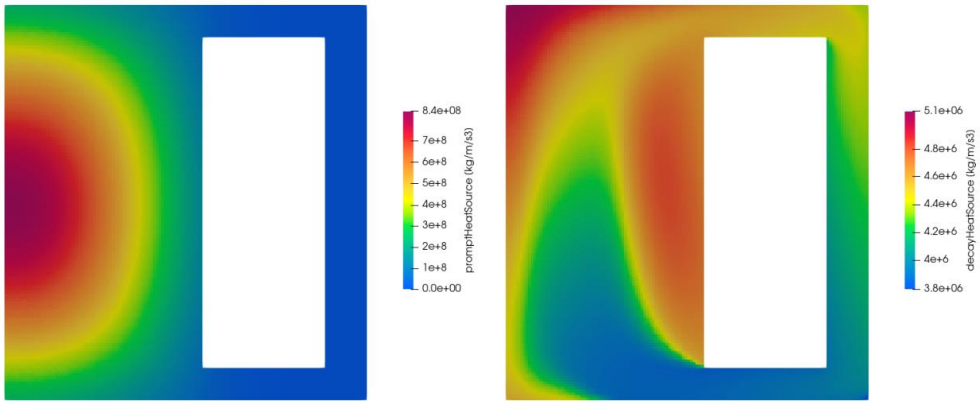

Selection of physical models

For the gas phase, the turbulent closure terms are set to zero, i.e., a 'laminar' turbulence model in OpenFOAM is selected. For the salt phase the turbulent closure terms are calculated using the k-epsilon model. Because the mesh is not wall resolving, standard OpenFOAM wall models are used for k and epsilon.

The gas phase is constituted by helium, which is assumed to behave as a compressible ideal gas. Its mole weight is set to 4 g/mol and its viscosity to $4.6913 \cdot 10^{-5}$ kg/m/s. The mass density of the salt is set to a constant value of 4215 kg/m^3, which corresponds to its mass density at 1000 K. This is expected to be close to the mean temperature of the reactor inventory. The constant salt density leads to a lack of natural circulation in the system, possibly affecting the flow pattern in the vessel. Also viscosity is set to a constant value, being 0.01 kg/m/s.

The two-fluid model's interfacial mass, momentum and energy transfer terms are closed as follows:

- It is assumed that no mass transfer occurs between helium bubbles and salt, meaning that helium does not condense onto the salt and salt does not evaporate into the bubbles.
- Heat transfer between bubbles and salt is based on the Ranz-Marshall correlation (15) (where Sh becomes Nu, i.e., the Nusselt number) as given above. Preliminary simulations showed that the heat transfer between salt and gas is so quick that virtually anywhere the temperature difference between salt and gas is very small, within tenths of Kelvin. Thus, the choice of heat transfer model between the two phases is not important.
- For the momentum transfer between salt and bubbles, we use the Schiller-Naumann model [23] for drag, virtual mass force with a standard coefficient of 0.5, the turbulent dispersion model of Lopez de Bertodano et al. [24] and a wall-damped lift model of Tomiyama et al. [25]. Where needed, bubbles are assumed to be perfectly spherical.

The LogMoM model requires the selection of a break-up kernel and a coalescence kernel. For break-up we use the model of Luo & Svendsen [26] with σ = 0.07197, 5 Gauss-Hermite quadrature points and 5 Gauss-Legendre quadrature points. For the coalescence kernel we use the one of Prince & Blanch [27] including both turbulent and buoyant coalescence, and with 5 Gauss-Hermite quadrature points. As

closing moments in LogMoM we use the zeroth (number), second (interfacial area) and third (volume) moments.

As outlined above, the particle phase is modeled using a sectional representation of the free and captured particle populations. For each distribution we use 16 sections, that logarithmically map the diameter space in such a way that the first section is located at 1 Å and the last section at 1 μm, thus spanning four diameter decades each with four sections. For the particle velocity a 'local equilibrium' model is used. Particle diffusivity is given by the Stokes-Einstein model. The modeling of hydrodynamic and diffusional flotation rates and efficiencies is as discussed above.

Unlike Caruggi et al. [22], no full multi-physics simulation is performed in the sense that the neutronics part of the problem is completely ignored. Instead, steady-state 'prompt' and 'decay' power fields were obtained from [22], to model the heat deposition inside the salt. These two fields are shown in Figure 2.

Numerical setup

Time-accurate simulations are performed with an adaptive time step controlled by a Courant-Friedrich-Lewy (CFL) limit of 0.5. The pressure-velocity system is solved in a segregated way using OpenFOAM's standard PIMPLE algorithm, with two outer iterations and three inner ones. In the first two inner iterations, the pressure equation is solved such that the residual has decreased by two decades. In the final inner iteration, the pressure equation is solved to an absolute tolerance level of 10^{-5}. The preconditioned conjugate gradient solver is used for the pressure equation. All other equations are solved using OpenFOAM's 'smoothSolver', all to an absolute tolerance level of 10^{-5}. No under- or over-relaxation is applied, so that simulation results are, in principle, time-accurate (although we mostly look at steady-state solutions of the salt-gas mixture).

Time derivatives are discretized using a mix of forward and backward Euler schemes, where the backward scheme is preferred in favor of the forward scheme if terms can be taken implicitly with respect to the main solution variable, for stability. The convective terms in the momentum and energy equation are discretized using OpenFOAM's standard 'limitedLinear' scheme. The convective terms in the k and epsilon equations are discretized using the first order upwind scheme, for stability. All other convective terms, including that of the void fraction, the zeroth and second moment of the bubble size distribution and the sectional free and captured particle concentrations, are discretized using the Van Leer scheme [28]. Laplacians, face interpolations and surface-normal gradients are all calculated using linear schemes without any non-orthogonality corrections because the computational grid is fully orthogonal.

Figure 3: Steady state solution for the axial velocity (top left), radial velocity (top right), salt temperature (bottom left) and pressure (bottom right), calculated for φ = 10 g/s and d_{in} = 1 mm.

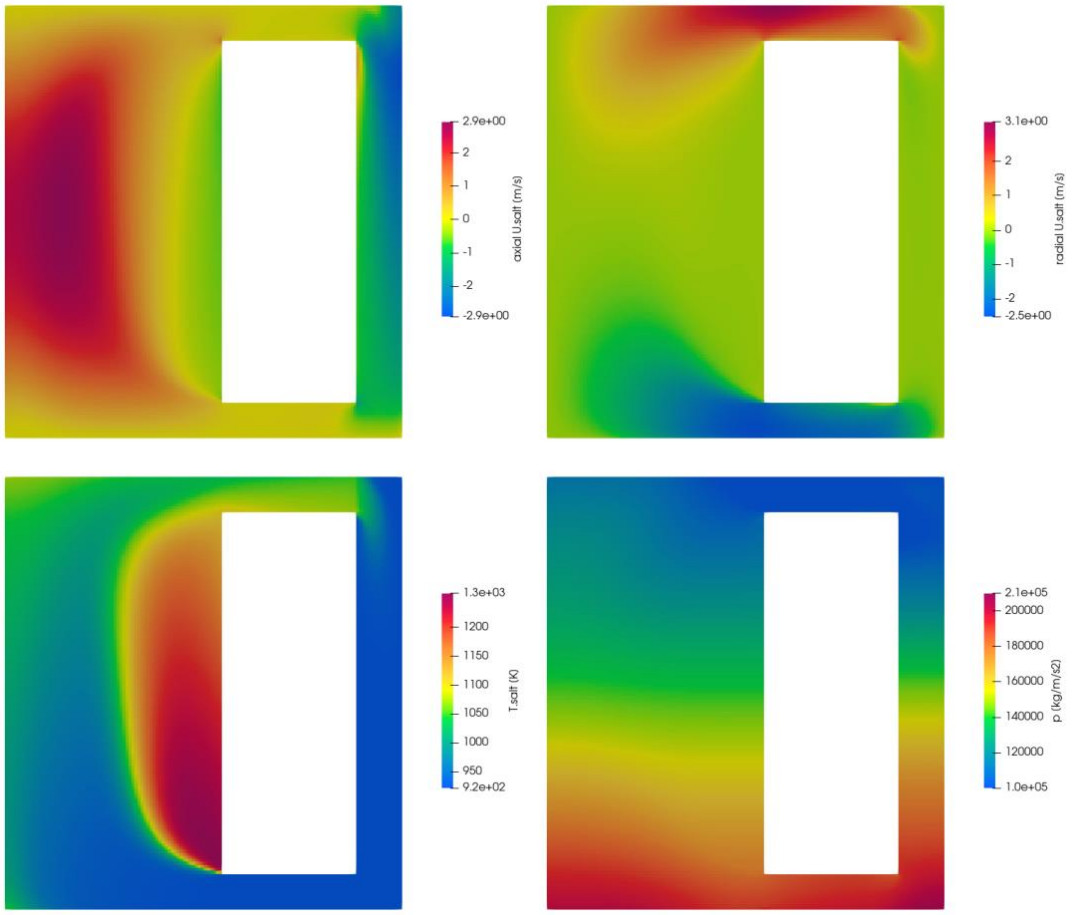

Simulation results and analysis

The goal of performing flotation simulations in the MSFR is to compute the cycle time of noble metals in the reactor, as a function of operational conditions. The key parameter to control noble metal content in the reactor is the mass flow rate φ of helium bubbles. One could envision the inlet bubble size as a secondary parameter. However, we will later show that the inlet bubble size has negligible influence on the mean particle size inside the reactor vessel, because the bubble size distribution rapidly adjusts to a mean bubble size that depends solely on the interplay of void fraction, coalescence and break-up but not on bubble size history. Thus, the only parameter to the problem is the helium mass flow rate.

In principle, we should perform transient simulations of particle formation, particle growth by coagulation and particle removal by bubbles. However, in [7] it was shown that the establishment of particle size distribution equilibria can, as a function of a single parameter Π (being the ratio between growth and removal time scale), take extremely long, even up to years for small values of Π. Such long operation times are infeasible for full transient CFD simulations. Moreover, in order to model particle growth a numerical method to solve the coagulation equation (e.g., see [29]) should be implemented, which is currently not done. Thus, the following alternative simulation strategy is adopted:

1. The main idea is to start from equilibrium size distributions that follow from theory, and to compute cycle times from the decay of such initial particle size distributions by bubble removal, without production or growth of new particles. As shown in [7], the equilibrium size distribution depends on parameter Π. In turn, Π depends on the interfacial area concentration of bubbles which is not known a priori and is a function of the helium mass flow rate. Thus, we must first compute the dependence of Π, averaged over the reactor vessel volume, on the mass flow rate φ, using our CFD model.
2. Once this dependence is known, an initial equilibrium size distribution of free particles can be calculated for any mass flow rate φ from theory [7]. Starting from such an initial condition, the rate of decay of total noble metal particle inventory as a function of time gives an estimate of the cycle time of noble metals in the MSFR. This cycle time can be compared with the theoretical one, in order to establish an interpretation of the role that both spatial inhomogeneity and hydrodynamic flotation play—physics that were neglected by the theory.

In this Section, we will discuss the simulation results of these two steps.

Figure 4: Steady state solution for the void fraction (top left), Sauter mean bubble diameter (top right), salt turbulent kinetic energy (bottom left) and salt turbulent viscosity (bottom right), calculated for φ = 10 g/s and d_{in} = 1 mm.

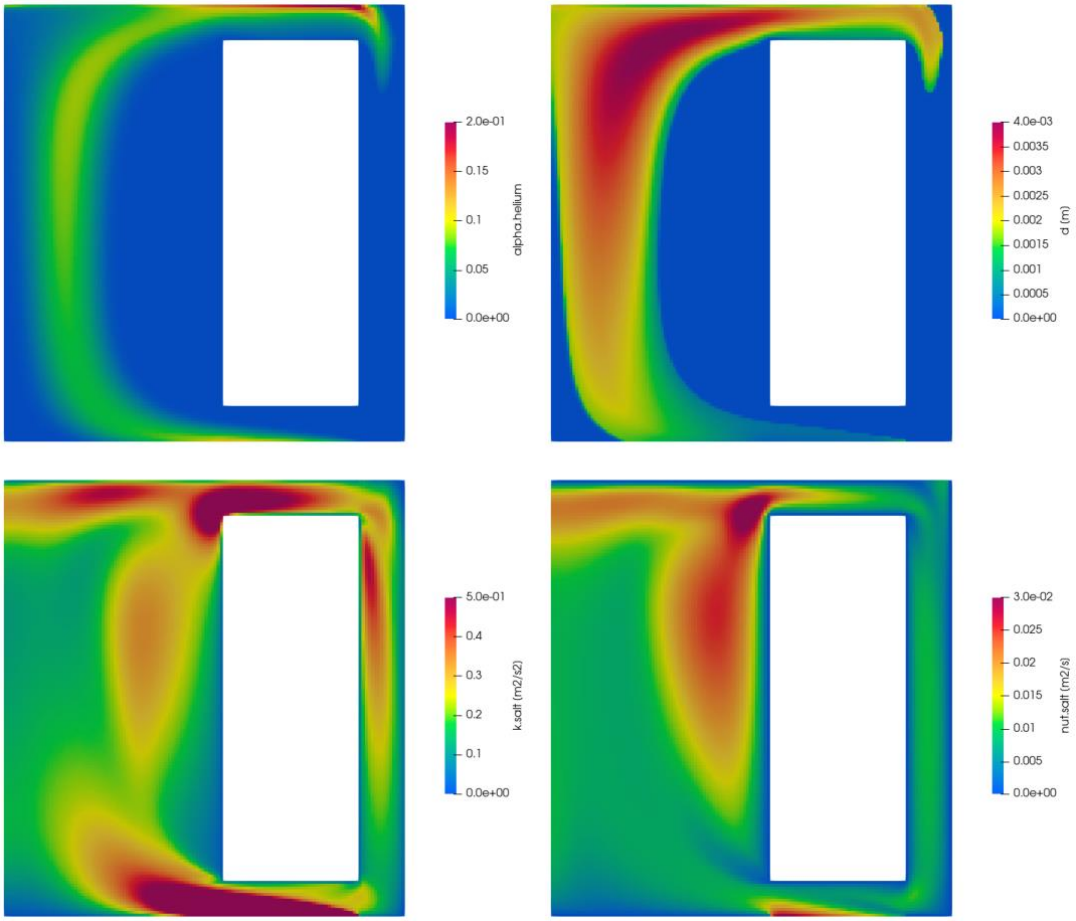

Figure 5: Reactor cavity volume-averaged void fraction and Sauter mean bubble diameter calculated for a range of mass flow rates and three inlet Sauter mean bubble diameters.

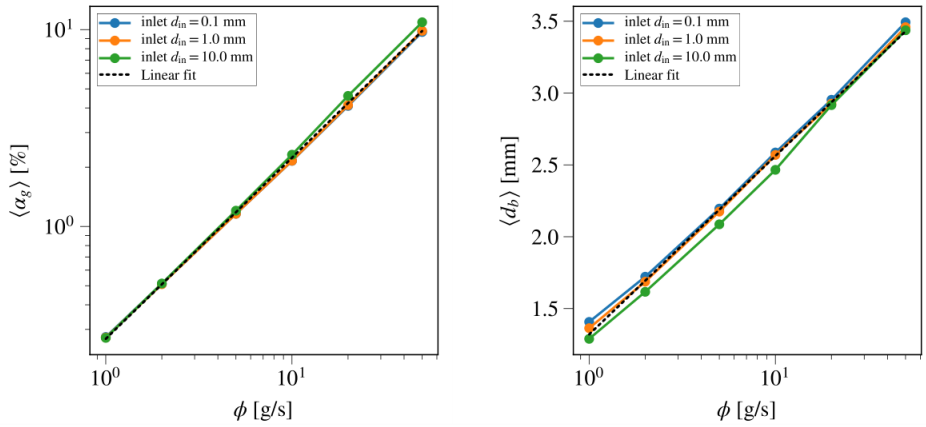

Preliminary simulations without noble metal particles

We perform preliminary simulations of the complex bubble-salt flow in the two-dimensional simplified representation of the MSFR geometry. For a range of inlet bubble diameters d_{in} and helium mass flow rates φ (defined in terms of the full geometry, not the wedge geometry), the steady-state vessel volume-average void fraction and bubble Sauter mean diameter are calculated. Note that the volume flow rate of helium depends on the pressure, which is the result of the static pressure of salt which is held at atmospheric pressure at the outlet to the expansion tank, see Figure 1. This leads to a pressure of roughly 2 bars at the inlet, although the exact value depends on the gas holdup in the vessel.

Figure 3 and 4 show the steady state solution variables at t = 100 s calculated using a helium mass flow rate of 10 g/s and an inlet Sauter mean bubble diameter of 1 mm. The calculation of the Sauter mean bubble diameter is not very accurate (nor very relevant) in low void fraction regions. Its value is set to zero in areas with void fractions below 0.1%. It can be observed from the temperature plot that the heat exchanger reduces the salt temperature back to an inlet temperature of approximately 920 K. Also the removal of bubbles is seen to be effective, so that no re-circulation of bubbles is established. The bubble diameter is seen to grow, which is the result of isothermal expansion due to reduced pressures. Moreover, the bubble size distribution is modified by the interplay of break-up and coalescence, which, in turn, depends on salt turbulence. The salt turbulence, expressed by the turbulent kinetic energy and turbulent viscosity fields, is seen to be highly non-uniform in the reactor vessel as a result of its geometry. The CFD model is capable of capturing these spatial effects, and the influence of the change of the bubble size distribution on the flotation efficiency, which will be discussed below.

From the simulations results we can calculate a volume-average void fraction and Sauter mean diameter in the reactor cavity. We define these two quantities as

$$\langle \alpha_g \rangle = \frac{1}{V_{\text{cav}}} \int_{V_{\text{cav}}} \alpha_g \mathrm{d}\mathbf{x} \qquad \text{and} \qquad \langle d_b \rangle = \frac{1}{\langle \alpha_g \rangle V_{\text{cav}}} \int_{V_{\text{cav}}} \alpha_g d_b \mathrm{d}\mathbf{x} \tag{16}$$

where V_{cav} is the reactor cavity volume as indicated in Figure 1. Figure 5 shows the two volume-averaged quantities, calculated at steady state for a range of helium mass flow rates and three inlet Sauter mean

bubble diameters. Clearly, both quantities are quite independent of the choice of inlet diameter, suggesting that break-up and coalescence re-organize bubbles sufficiently quickly so that the inlet diameter has no significant influence on the volume-average result. On the other hand, both the volume-averaged void fraction and bubble diameter are seen to change noticeably with increasing helium mass flow rate. This is a trivial result for the void fraction, however, for the bubble diameter it is less obvious, as it results from a complex interplay of the coalescence and break-up kernels depending on non-uniform void fraction and turbulence. The effect of coalescence and break-up can generally be understood by the observation that a larger concentration of bubbles increases the likelihood of coalescence and thus size.

Also shown in Figure 5 is a linear fit on both quantities, each averaged over the three inlet diameters. These linear fits give a correlation between helium mass flow rate and mean vessel void fraction on one hand, and helium mass flow rate and mean vessel bubble diameter on the other. In turn, these two quantities can be fed into the definition of parameter Π, yielding the vessel volume-average parameter

$$\langle \Pi \rangle = \frac{3\mathrm{Sh}}{\pi b} \frac{\langle \alpha_g \rangle}{\langle d_b \rangle^2} \sqrt{\frac{K}{F}}, \tag{17}$$

with initial noble metal particle diameter b, coagulation constant K and noble metal particle production rate F, see [7]. The Sherwood number is, through the Ranz-Marshall relation (15), a function of bubble Reynolds number, for which a correlation is given in [7] as function of the bubble diameter, and the particle Schmidt number which is estimated in [7] too. Using the resulting Sherwood number function along with the fits shown in Figure 5 for $\langle \alpha_g \rangle$ and $\langle d_b \rangle$ and the values of b, F and K (also given in [7]), gives the vessel volume-averaged parameter $\langle \Pi \rangle$ which is shown in Figure 6 as a function of helium mass flow rate. A linear fit in the double logarithmic space as displayed in Figure 6 yields

$$\langle \Pi \rangle = 0.512 \phi^{0.700}. \tag{18}$$

This function, then, is used as the sole input to the model presented in [7] that predicts the equilibrium noble metal size distribution. In turn, the outcome of that model which, through $\langle \Pi \rangle$, has become a function of φ, is used as the initial condition for the free particle population for the flotation CFD calculations presented next.

Figure 6: The reactor vessel volume-average parameter ⟨Π⟩ as function of the helium mass flow rate for the simplified two-dimensional geometry of the MSFR.

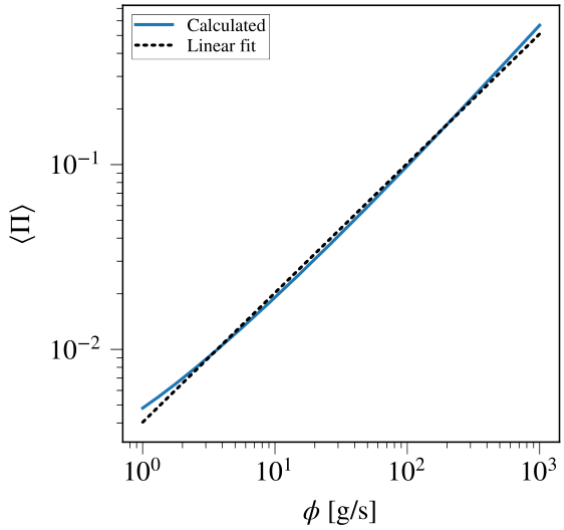

Noble metal particle flotation simulations

From the model presented in [7] and the function for ⟨Π⟩ (18) the initial free particle population $n_f(d)$ at time t = 0 can be constructed. For large values of ⟨Π⟩ at high helium mass flow rates, the initial free particle population will have predominantly small particles while for small values of ⟨Π⟩ at low helium mass flow rates the initial free particle population will have predominantly much larger particles. Thus, when we increase the helium mass flow rate, we automatically decrease the initial mean noble metal particle sizes because at high helium mass flow rates the equilibrium particle size distribution predicted by theory will not grow significantly as a result of more effective flotation.

Next, we calculate the initial sectional concentrations using

$$N_{i,f} = \int_{y_i}^{y_{i+1}} n_f(d)\mathrm{d}d, \tag{19}$$

with y_i the lower integration limit of section i and y_{i+1} the upper integration limit of section i. These limits are set midway between the two adjacent representative sectional sizes in logarithmic space, i.e., $y_i = \sqrt{(d_{i-1}d_i)}$ with the exception of y_1 and y_{n+1} which are set to zero and infinity, respectively.

Figure 7: Total noble metal mass inventory in the reactor scaled by its initial amount as a function of time for eight values of the helium mass flow rate (left) and the corresponding cycle times (right).

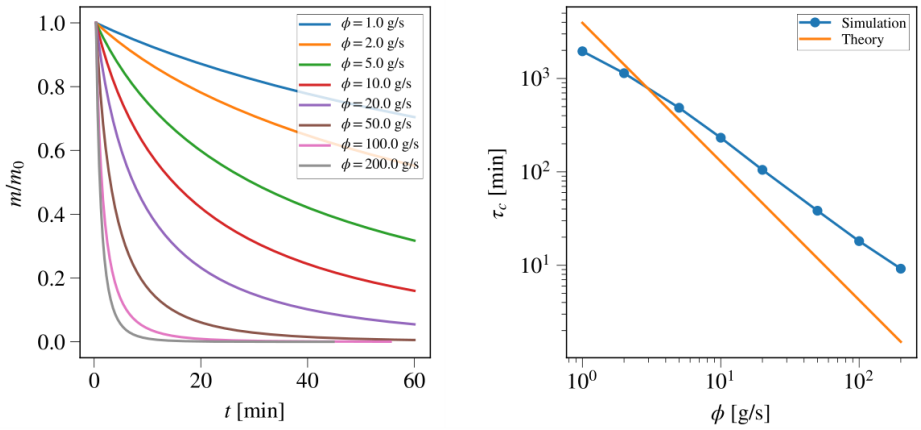

Starting from a fully developed steady-state solution in terms of the salt-helium mixture, we initialize the appropriate equilibrium free noble metal particle population and simulate the transfer of that free particle population to the captured particle population by means of flotation. We recall that the removal rate of particles as predicted by the CFD simulation may differ from the theory because of spatial inhomogeneity, but also because the CFD simulation incorporates hydrodynamic flotation. Thus, the initial free particle population is only an estimate and does not necessarily reflect exact steady-state conditions subject to the CFD model. Simulations are performed over the course of one hour, in order to establish significant particle removal for all considered mass flow rates. Figure 7 (left) shows the total noble metal mass inventory m in the reactor, scaled by its initial value, as a function of time, for eight values of the helium mass flow rate. The mass inventory is calculated as the third moment of the free particle size distribution, i.e.,

$$m = \frac{\rho_p \pi}{6} \int_0^\infty d^3 n_f(d) \mathrm{d}d \approx \frac{\rho_p \pi}{6} \sum_i d_i^3 N_{i,f} \tag{20}$$

It is clearly observed in Figure 7 (left) that low mass flow rates lead to slow particle removal while for higher mass flow rates the removal becomes progressively more efficient, as a result of the presence of more interfacial area. We may quantify the rate of removal by calculating the cycle time τ_c that generates the best match between the numerical data and an exponential decay function given by

$$\frac{m}{m_0} = \exp\left(-\frac{t}{\tau_c}\right). \tag{21}$$

Since our simulation time is 1 h, we can thus calculate the cycle time as $\tau_c = -1/\log(m_{1\mathrm{h}}/m_0)$ in units of hours, where $m_{1\mathrm{h}}$ is the total noble metal mass inventory after 1 h of simulated time. The cycle times that result from this definition are shown in Figure 7 (right) for a range of helium mass flow rates. Also shown is the theoretical prediction. From this plot, we can draw three conclusions:

- For high helium mass flow rates the initial particle population contains only small particles that are not susceptible to hydrodynamic flotation and only to diffusional flotation, the latter upon

which the theoretical prediction is exclusively based. Thus, at high flow rates the difference between theory and numerical prediction are related to the diffusion term and not to the hydrodynamic flotation term. We observe that the numerically calculated cycle time is almost a decade larger than the theoretical one at the highest flow rate shown, which is significant. One reason for this is that the parameter $\langle \Pi \rangle$ is based on the reactor vessel cavity only, while free particles can also enter the pump and heat exchanger volume which comprises a significant amount of volume (due to radial expansion of the geometry) but where no bubbles are present giving free particles more chance to avoid removal. Also, as can be seen in Figure 4, bubbles are concentrated locally in an upward plume. Particles in that plume are removed efficiently, but particles outside it largely avoid removal until they diffuse into the plume. This diffusional processes is slow, particularly for large particles which hold most mass. Moreover, mean bubble size is seen to be strongly varying in space too, changing the local flotation characteristics with respect to the vessel volume averaged one.

- We also observe in Figure 7 that the slope of the cycle time curve is slightly steeper in the theoretical line, even at large mass flow rates. This can be explained by the fact that in the theory the particle Sherwood number is assumed to be independent of particle size while in reality it carries a weak dependence ($\sim d^{-1/3}$). This dependence is considered in the CFD simulation, but is ignored in theory, resulting in a slightly steeper slope in the theoretical cycle time prediction.
- At lower helium mass flow rates the difference in cycle time prediction decreases, and at some point changes sign; for small flow rates the cycle time becomes smaller than the theoretical one. This can be attributed to the modeling of hydrodynamic flotation and the enhancement in removal rates it results in for large particles. Such large particles are only present for low helium mass flow rate runs, because for low mass flow rates the initial noble metal particle size distribution contains significantly larger particles.

The results above are ‘integral’ quantities in the sense that we considered the decay rate of the total noble metal mass inventory. Instead, we can also look at the decay rate of the sixteen individual free particle sections, for the set of eight simulated mass flow rates giving 128 data points. Moreover, from each such point a corresponding ‘partial’ cycle time can be computed in the same way as before, but now based on the fraction of free particles in section i, $N_{i,f}(1\text{h})/N_{i,f}(0)$, giving the partial cycle time as a function of both helium mass flow rate and noble metal particle size. This, then, is shown in Figure 8. It can be seen that at constant helium mass flow rate, the cycle time increases monotonically until particle sizes of about 500 nm as a result of decreased Brownian diffusivity. Above roughly 500 nm, hydrodynamic flotation is seen to become more effective, decreasing the cycle time in turn. We note, however, that the net cycle time of noble metal mass inventory is an integral over all sizes weighted by the free particle population. This is what is discussed above and presented in Figure 7, and represents the main finding of this work.

Figure 8: Partial cycle time as a function of both helium mass flow rate and noble metal particle size.

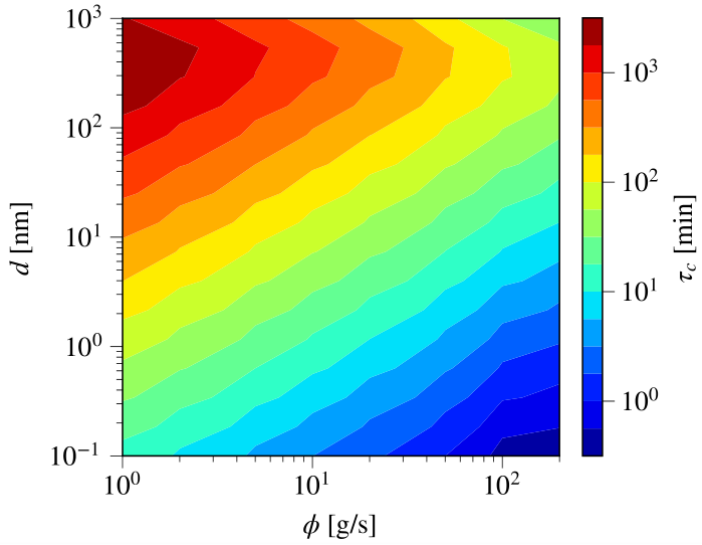

Conclusions

This work has investigated the hydrodynamic and diffusional flotation of noble metal particles in an MSR, by CFD simulation of a simplified reactor geometry. Theory shows that at low bubble flow rates it takes very long to establish equilibrium particle distributions, which is not feasible to be simulated by CFD. Instead, we imposed approximate equilibrium size distributions that were calculated by theory as initial condition, and simulated the removal of member particles of that initial size distribution in time. Based on the decay rate of noble metal mass, a cycle time was calculated for a range of bubble mass flow rates. It was shown that simulated cycle times are almost an order of magnitude larger at very high bubble flow rates as compared to theory, suggesting that inhomogeneity of the reactor, which is not accounted for in the theory, plays an important role. Several reasons for this were discussed. Most importantly, the plume of bubbles and the bubble sizes contained within are very non-uniform and are expected to change flotation characteristics significantly. From this we can conclude that it is important to simulate an accurate representation of the real MSFR geometry and that a two-dimensional simplified geometry may not be sufficient for the calculation of accurate removal rates. Moreover, it was observed that the slope of the cycle time curve was slightly steeper in the simulations, attributed to the fact that the size dependence of the Sherwood number is ignored in the theory.

Finally, we concluded that at low bubble flow rates the initial particle distribution (predominantly containing large particles) was subject to hydrodynamic flotation too, reducing the cycle time as compared to the theory which only includes diffusional flotation. However, large particles can only arise in the MSR after very long steady-state operational times, which may be unrealistic.

Funding

This project has received funding from the Euratom research and training program 2014–2018, under grant agreement No. 847527.

Data

The data that support the findings of this study are openly available in Zenodo at https://doi.org/10.5281/zenodo.7628854.

Disclaimer

The content of this paper does not reflect the official opinion of the European Union. Responsibility for the information and/or views expressed therein lies entirely with the authors.

References

[1] V. Habiyaremye, E.M.J. Komen, J.G.M. Kuerten, and E.M.A. Frederix. Modeling of bubble coalescence and break-up using the log-normal method of moments. Chemical Engineering Science, page 117577, 2022.

[2] E. Merle-Lucotte, D. Heuer, M. Allibert, M. Brovchenko, N. Capellan, and V. Ghetta. Launching the thorium fuel cycle with the molten salt fast reactor. In Proceedings of ICAPP, volume 2, 2011.

[3] R.J. Kedl. Migration of a class of fission products (noble metals) in the molten-salt reactor experiment. Technical report, Oak Ridge National Lab., Tenn.(USA), 1972.

[4] S. Delpech, E. Merle-Lucotte, D. Heuer, M. Allibert, V. Ghetta, C. Le-Brun, X. Doligez, and G. Picard. Reactor physic and reprocessing scheme for innovative molten salt reactor system. Journal of Fluorine Chemistry, 130(1):11–17, 2009.

[5] N. Mishchuk, J. Ralston, and D. Fornasiero. The analytical model of nanoparticle recovery by microflotation. Advances in Colloid and Interface Science, 179:114–122, 2012.

[6] A.V. Nguyen and H.J. Schulze. Colloidal Science of Flotation, volume 118. CRC Press, 2003.

[7] E.M.A. Frederix. Estimates of noble metal particle growth in a molten salt reactor. Colloids and Surfaces A: Physicochemical and Engineering Aspects, page 130167, 2022.

[8] E.M.A. Frederix. Helium bubbling literature review, model development and model application. Technical report, NRG, 2018.

[9] E. Cervi, S. Lorenzi, A. Cammi, and L. Luzzi. An Euler-Euler multiphysics solver for the analysis of the helium bubbling system in the MSFR. In 26th International Conference Nuclear Energy for New Europe, 2017.

[10] M. Ishii and T. Hibiki. Thermo-fluid dynamics of two-phase flow. Springer Science &Business Media, 2010.

[11] D.A. Drew and S.L. Passman. Theory of multicomponent fluids, volume 135. Springer Science & Business Media, 2006.

[12] S.K. Friedlander. Smoke, dust and haze: Fundamentals of aerosol behavior. 1977.

[13] D.L. Marchisio and R.O. Fox. Computational models for polydisperse particulate and multiphase systems. Cambridge University Press, 2013.

[14] D. Ramkrishna. Population balances theory and applications to particulate systems in engineering. 2000.

[15] R.H. Yoon and G.H. Luttrell. The effect of bubble size on fine particle flotation. Mineral Procesing and Extractive Metallurgy Review, 5(1-4):101–122, 1989.

[16] Z. Dai, D. Fornasiero, and J. Ralston. Particle–bubble attachment in mineral flotation. Journal of colloid and interface science, 217(1):70–76, 1999.

[17] W.E. Ranz and W.R. Marshall. Evaporation from drops. Chemical Engineering Progress, 48(3):141–146, 1952.

[18] M.W. Rosenthal, R.B. Briggs, and P.R. Kasten. Molten-salt reactor program semiannual progress report for period ending February 28, 1969. Technical report, Oak Ridge National Lab.(ORNL), Oak Ridge, TN (United States), 1969.

[19] E.L. Compere, S.S. Kirslis, E.G. Bohlmann, F.F. Blankenship, and W.R. Grimes. Fission product behavior in the molten salt reactor experiment. Technical report, Oak Ridge National Lab.(ORNL), Oak Ridge, TN (United States), 1975.

[20] E.M.A. Frederix, T.L.W. Cox, J.G.M. Kuerten, and E.M.J. Komen. Poly-dispersed modeling of bubbly flow using the log-normal size distribution. Chemical Engineering Science, 201:237–246, 2019.

[21] H. Rouch, O. Geoffroy, P. Rubiolo, A. Laureau, M. Brovchenko, D. Heuer, and E. Merle-Lucotte. Preliminary thermal–hydraulic core design of the molten salt fast reactor (MSFR). Annals of Nuclear Energy, 64:449–456, 2014.

[22] F. Caruggi, A. Cammi, E. Cervi, A. Di Ronco, and S. Lorenzi. Multiphysics modelling of gaseous fission products in the molten salt fast reactor. Nuclear Engineering and Design, 392:111762, 2022.

[23] R. Clift, J.R. Grace, and M.E. Weber. Bubbles, drops, and particles. Courier Corporation, 2005.

[24] M. Lopez de Bertodano, R.T. Lahey, and O.C. Jones. Phase distribution in bubbly two-phase flow in vertical ducts. International Journal of Multiphase Flow, 20(5):805–818, 1994.

[25] A. Tomiyama, H. Tamai, I. Zun, and S. Hosokawa. Transverse migration of single bubbles in simple shear flows. Chemical Engineering Science, 57(11):1849–1858, 2002.

[26] H. Luo and H.F. Svendsen. Theoretical model for drop and bubble breakup in turbulent dispersions. AIChE Journal, 42(5):1225–1233, 1996.

[27] M.J. Prince and H.W. Blanch. Bubble coalescence and break-up in air-sparged bubble columns. AIChE journal, 36(10):1485–1499, 1990.

[28] B. Van Leer. Towards the ultimate conservative difference scheme. V. A second-order sequel to Godunov's method. Journal of Computational Physics, 32(1):101–136, 1979.

[29] S. Kumar and D. Ramkrishna. On the solution of population balance equations by discretization–I. A fixed pivot technique. Chemical Engineering Science, 51(8):1311–1332, 1996.

[30] E.M.A. Frederix. Dataset for CFD4NRS-9 conference paper "Simulation of noble metal particle growth and removal in the molten salt fast reactor". https://doi.org/10.5281/zenodo.7628854.